Supporting Information for:

Coordination coupling enhanced two-photon absorption of ZnS-based nanohybrid for two-photon microscopy imaging in HepG2

Lin Kong, Xiao-he Tian, Yuan-hao Gao, Hui Wang, Qiong Zhang, Jia-xiang Yang, Hong-ping Zhou, Sheng-yi Zhang, Yu-peng Tian

Contents:

S1. Nonlinear optical measurements

The data of δ was calculated by comparing the TPEF intensity to that of fluorescein in NaOH solution (aq, 0.1 mol/L) (pH = 11) [S1] at different exciting wavelength according to equation (S1)

$$\delta = \delta_{ref} \frac{\Phi_{ref}}{\Phi} \frac{C_{ref}}{C} \frac{n_{ref}}{n} \frac{F}{F_{ref}} \quad \text{(S1)}$$

In this equation,[S2] the subscripts *ref* referred to the reference molecule, which was fluorescein. δ was the TPA cross-section value, c was the concentration of the solution, n was the refractive index of the solution, F was the TPEF integral intensities of the solution emitted at the exciting wavelength, and Φ was the fluorescence quantum yield.

To determine the concentration of ZnS_2L component in the hybrid to calculate the δ value, the hybrid was dissolved in alkaline medium, in this process ZnS core was dissolved and ZnS_2L component was dissociated. As ZnS_2L was synthesized from alkaline medium, the alkaline medium used here will not destroy the structure of it. The dissociated ZnS_2L component was then extracted from water medium using CH_2Cl_2. The possible composition of ZnS_2L in the hybrid was captured through UV-Vis test and analyzed by the absorbance superposition principle.

The δ_{ref} value of reference equalled to 38, which was taken from the literature.[S1,S3] The TPA spectra were drawn through the calculated δ data as y axis and the changed wavelength as x axis.

Based on Z-scan determination method, nonlinear absorption coefficient β, the nonlinear refractive index γ, the real and imaginary parts of $\chi^{(3)}$ of third-order nonlinear susceptibility were determined simultaneously, using the so-called closed-aperture and open-aperture conditions, respectively. The experimental errors were estimated to be ± 10% from the variations of laser energies and sample concentrations.[S4] The calculated formula were listed in the supporting information.

Based on Z-scan determination method, the real and imaginary parts of $\chi^{(3)}$ were determined simultaneously, using the so-called closed-aperture and open-aperture conditions, respectively. Nonlinear absorption coefficient β was measured by open aperture Z-scan technique. For the open aperture, the normalized transmittance as a function of the position along the z axis can be written as formula (S2)

$$Tz = \sum_{m=0}^{\infty} \frac{[-q(z)]^m}{(m+1)^{3/2}}, \text{ where } q(z) = \frac{\beta I_0 L_{eff}}{[1+(z/z_0)^2]\alpha} \qquad \text{(S2)}$$

Z_0 was the diffraction length of the beam, I_0 was the intensity of the light at focus, L_{eff} was the effective length of the sample, α was the linear absorption coefficient at the wavelength used.[S5]

For the close aperture, the calculation of the nonlinear refractive index γ fitting can be done as formula (S3)

$$T_{P-V} = 0.406(1-S)^{0.25}|\Delta\Phi|, \text{ where } |\Delta\Phi| = KL_{eff}\gamma I_0 \qquad \text{(S4)}$$

$\Delta T_{P\text{-}V}$ was the difference between normalized transmittance values at valley and peak positions from the closed aperture scan. s was the fraction of the transmitted beam through the aperture the data was 0.20 in the experiment. $\Delta\Phi_0$ was the on-axis nonlinear phase shift and K was the wave vector.

The third-order nonlinear susceptibility ($\chi^{(3)}$) was also determined through the close aperture Z-scan method.[S6] The data of real part of third-order nonlinear susceptibility $Re(\chi^{(3)})$ can be calculated by the experimental measurements of γ as formula (S5)

$$\mathrm{Re}\,\chi^{(3)}(esu) = \frac{\varepsilon_0 c^2 n_0^2 \gamma}{\pi} \qquad \text{(S5)}$$

where ε_0 was the vacuum permittivity, c was the light velocity in vacuum, n_0 was the linear refractive index.

The data of imaginary part of third-order nonlinear susceptibility $Im(\chi^{(3)})$ can be calculated by the data of β as formula (S6)

$$\mathrm{Im}\,\chi^{(3)}(esu) = \frac{\varepsilon_0 c^2 n_0^2 \lambda \beta}{4\pi^2} \qquad \text{(S6)}$$

S2. Illustration of the formation process of the hybrid particles

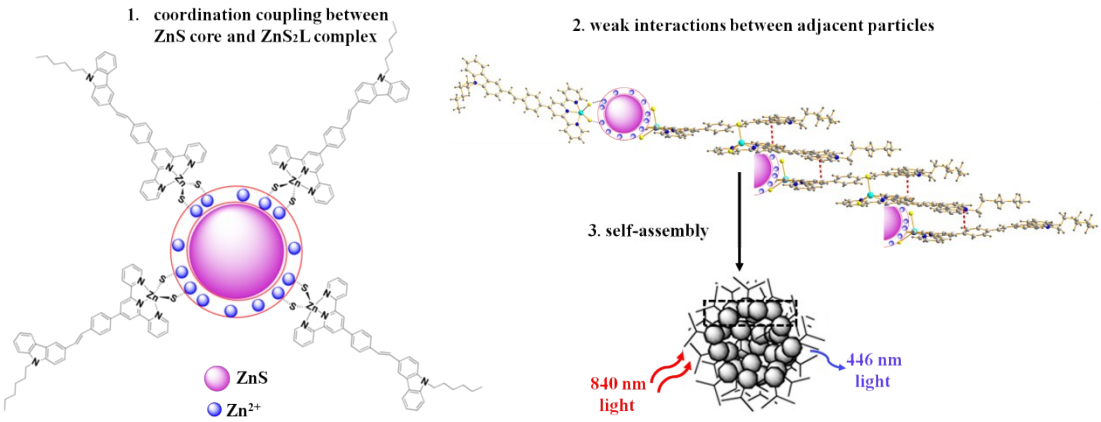

Figure S1 Illustration of the coordination coupling effect at the interface and the corresponding weak interactions between adjacent hybrid particles. The weak interactions between ZnS_2L molecules of adjacent hybrid particles were organized from the single crystal structure reported in reference 25.

S3. Characterization of bare ZnS, free ZnS_2L and the hybrid

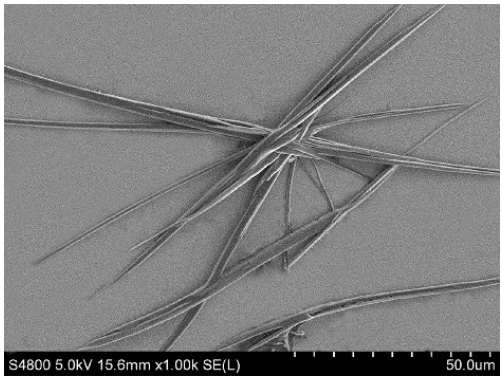

Figure S2 A general SEM view of ZnS_2L sisal prepared from EtOH-H_2O mixed solution

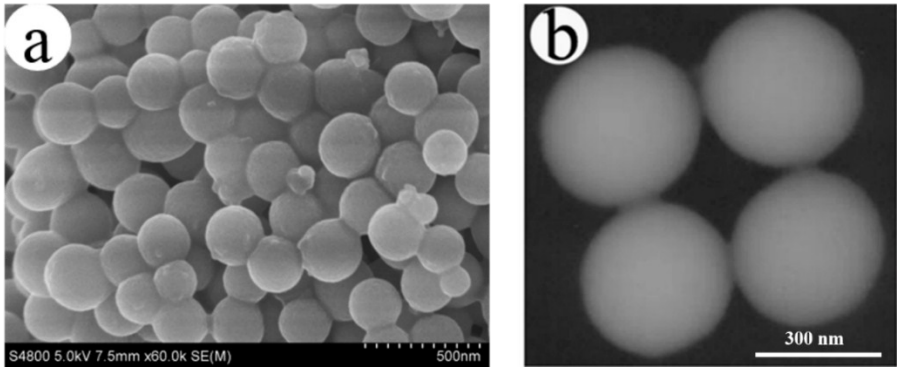

Figure S3 (a) SEM and (b) TEM images of bare ZnS prepared without ZnS_2L in this study, the samples were dispersed in EtOH solution.

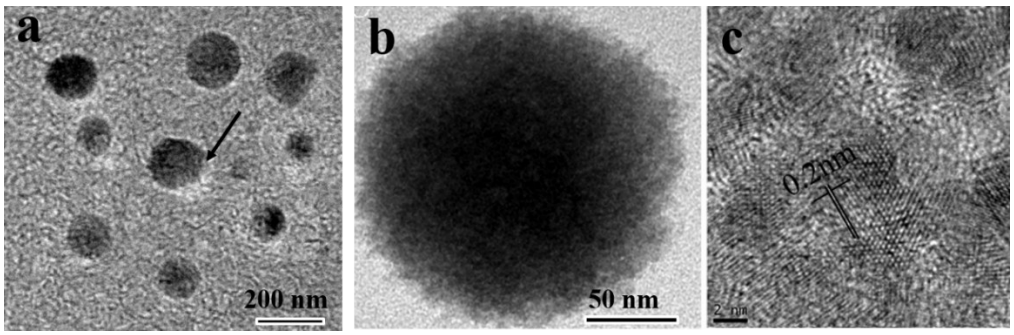

Figure S4 (a) TEM image of aggregated ZnS particles; b) TEM image of a typical aggregated ZnS particle showing the hybrid aggregated from small ZnS particles; c) typical HRTEM image of small ZnS particles. The samples were dispersed in EtOH solution.

The morphology of the hybrid can be directly visualized through SEM and TEM examination. High uniform nanospheres with a mean diameter of about 130 were observed. Moreover, it can also be seen from TEM image (Fig. S4) that the spherical aggregates of the hybrid were composed of small particles with the mean size being about 4 nm. The results of HRTEM image (Fig. S4c) and the black markers of the XRD pattern (Fig. S5) also revealed that these spherical hybrid particles were the zinc blende phase of ZnS. The average particle size, calculated from (111) reflection by the Scherrer equation, was approximately 4.0 nm, which was consistent with the HRTEM observations. Moreover, the red markers of the XRD pattern clearly revealed the existence of organic component, ZnS_2L, in the hybrid, the diffraction peaks of which (such as $12\bar{1}$, 02_2 and $32\bar{1}$) were identified through the single crystal structure of ZnS_2L.

The morphology of the nanohybrid was very different from that of bare ZnS and/or pure ZnS_2L, indicating that ZnS_2L and ZnS component were greatly affected during the hybridzation process. SEM images of ZnS_2L nanostructures were shown in Fig. S2, from which sisals were observed with dozens of micrometers in length. Bare ZnS prepared without ZnS_2L were spherical like structure with the diameter of about 300 nm (Fig. S3). The morphology changing revealed somewhat strong interactions between ZnS and ZnS_2L components in the nanohybrid.

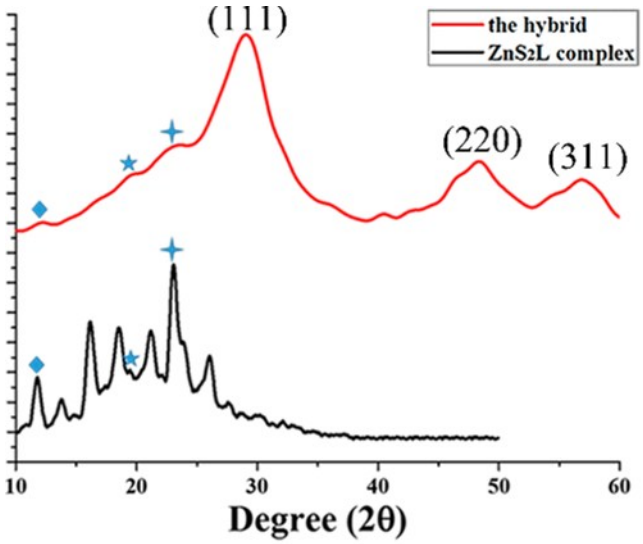

Figure S5 XRD pattern of ZnS_2L and the hybrid

The XRD pattern mentioned above revealed the existence of inorganic component ZnS and organic component ZnS_2L in the hybrid. Furthermore, the composition of the hybrid and intermolecular interactions between the two components were analyzed using far-IR (Fig. S7), Raman sacttering (Fig. S8), XPS (Fig. 2 in the main text) and energy dispersive X-ray spectroscopy (EDX, Fig. S9).

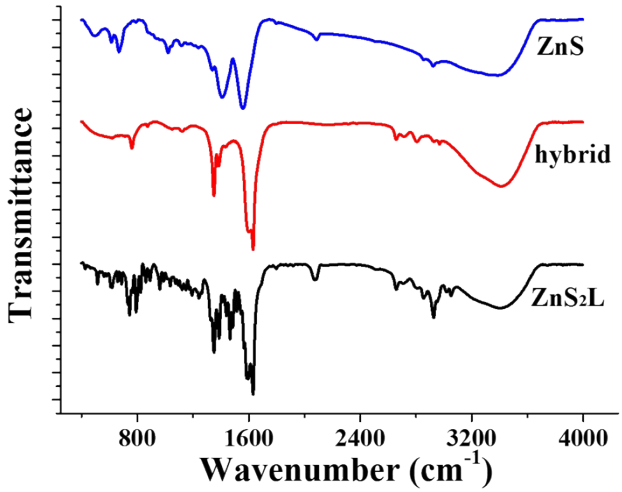

Figure S6 IR spectra of ZnS_2L, bare ZnS and the hybrid

The chemical composition of the spherical aggregates is examined using FTIR (Fig. S6). ZnS_2L exhibits strong bands at 1582, 1464 and 1380 cm^{-1}, respectively, which can be assigned to vibration of the terpyridyl moiety. Furthermore, the band at 474 cm^{-1} in Fig. S6 or 477 cm^{-1} in is attributed to the stretching vibration of Zn-S bond of the hybrid. The results suggest that the capping ZnS_2L reacts with ZnS particles at the interface.

Far-IR spectra exhibited bands at 513 and 403 cm^{-1} for ZnS_2L, which can be assigned to the vibration of Zn-N and Zn-S bond, respectively. However, the far-IR spectrum of the hybrid showed bands at 509 nm and 285 cm^{-1}, respectively. The bands showed bearing broadened, relatively stronger and bathochromic shift from that of ZnS_2L. The band at 285 cm^{-1} also showed an up-shift from that of bare ZnS prepared without ZnS_2L (271 cm^{-1}). The results further confirmed that the terminal sulfur atoms in ZnS_2L molecule covalently attached to ZnS particles at the interface, as well as that there was a somewhat larger delocalization system in the hybrid.[S7] The interactions between the

two terminal S atoms of ZnS_2L molecule and Zn atoms at the surface of ZnS particles led to increased π-conjugated degree of ZnS_2L molecule around S atoms, and brought about change of far-IR.

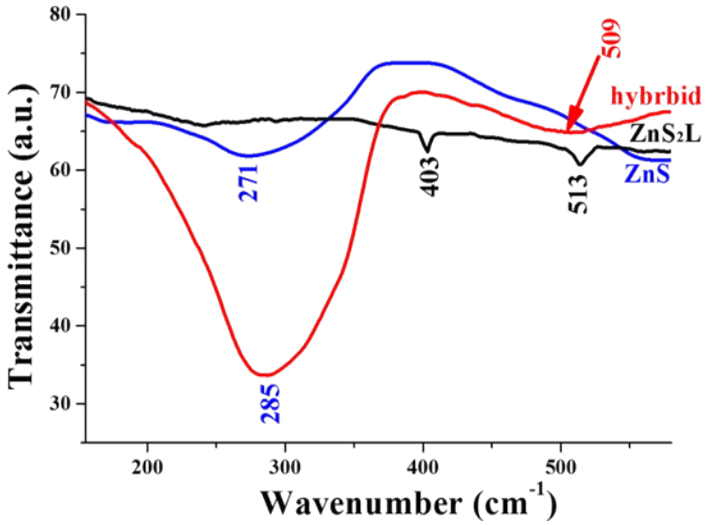

Figure S7 Far IR spectra of the bare ZnS, free ZnS_2L and the hybrid

Raman scattering spectra of the hybrid as shown in Fig. S8 clearly showed the interactions between the two components at the interface. The Raman sacttering band at 355 cm^{-1} can be considered as originating from the Zn-S bond, which was fit well with that of bare ZnS particels (349 cm^{-1}) and 351 cm^{-1} for ZnS_2L. The shift clearly showed the influerence of coordiantion coupling effect on the Raman sacttering band of the two components in the hybrid. The band at 422 cm^{-1} of the hybrid was originated from the Zn-N bond, which also appeared at 414 cm^{-1} for ZnS_2L. The bands at 1594 cm^{-1} to 938 cm^{-1} of the hybrid can be considered as from the the ring breathing of the benzene ring and the C=C stretching vibrations of ZnS_2L, which showed different extent of down-shift or up-shift.

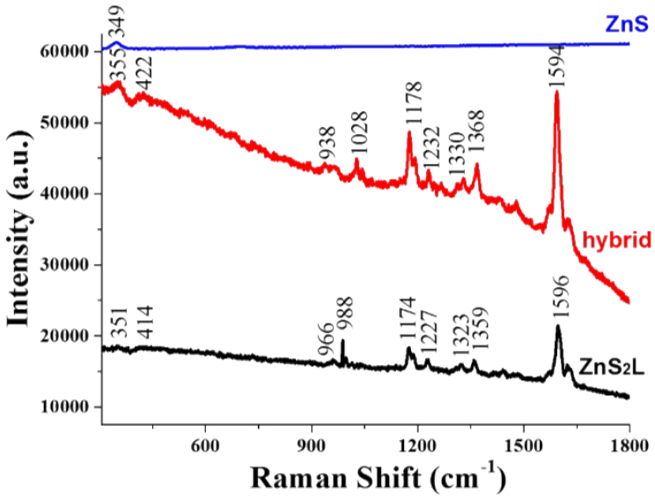

Figure S8 Raman scattering spectra of the bare ZnS, free ZnS_2L and the hybrid

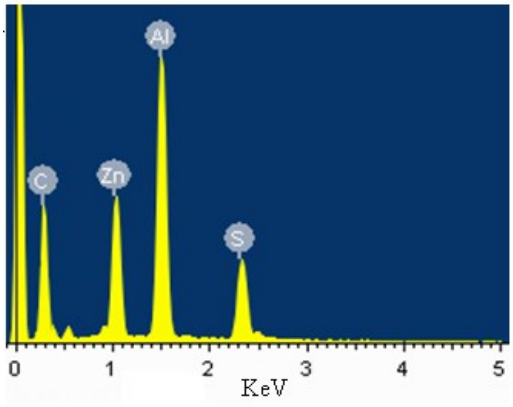

Figure S9 EDX spectrum of the hybrid shown in Fig. 2a

S4. Determination of binding constant from UV-vis titration data

Binding constant (*K)* was calculated according to the Benesi-Hildebrand equation.[S8] *K* was calculated following the equation stated below.

$$\frac{1}{\text{A-A}_0} = \frac{1}{K(\text{A}_{max} - \text{A}_0)[Zn^{2+}]} + \frac{1}{\text{A}_{max} - \text{A}_0}$$

Here A_0, A and A_{max} indicate the absorbance in absence of, at intermediate and at infinite concentration of metal ion respectively. The binding constant K is determined from the ratio of intercept and slope of Benesi-Hildebrand plot. If the plot of $1/[A\text{-}A_0]$ vs $1/[Zn^{2+}]$ gives a straight line indicating 1:1 complexation or $1/[A\text{-}A_0]$ vs $1/[M^{2+}]^2$ gives a straight line indicating 1:2 complexation between ligand and metal ion. In the present case the plot of $1/[A\text{-}A_0]$ vs $1/[M^{2+}]$ gives a straight line. Thus the stoichiometry

is 1:1 (ZnS_2L : Zn^{2+}). From the absorption spectral data, we have evaluated the bindding constant of ZnS_2L using Benesi–Hildebrand equation and it is found to be 2.86×10^4 $L \cdot mol^{-1}$.

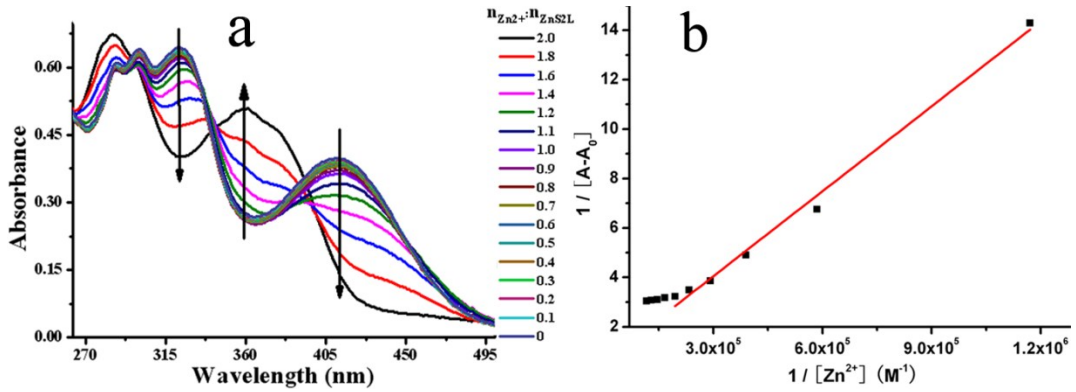

Figure S10 (a) UV-vis titration experiment of ZnS_2L ethanol solution in presence of Zn^{2+} with different equivalent; (b) Benesi-Hildebrand plot for 1:1 complexation of ZnS_2L with Zn^{2+} in EtOH/H_2O mixted solvent with *f*w = 90%.

S5. Linear optical properties

To further understand the change of fluorescence of the samples, the photoluminescence excitation (PLE) spectra of them were studied as shown in Fig. S11. For 528 nm emission band of ZnS_2L, the excitation bands centered at 326 nm and 416 nm. The latter may result from the whole ZnS_2L conjugated molecule while the former may result from a fluorescent fragment of the molecule such as carbazole unit. For 522 nm emission band of the hybrid, the excitation bands centered at 300 nm and 375 nm, which showed a clear blue-shift from that of ZnS_2L. The interactions between ZnS_2L moiety and ZnS particles through the two terminal S^{-1} atoms and Zn^{2+} ions at the interface were the main cause of the change, which can influence the whole conjugated structure of the ZnS_2L molecule. While for 416 nm emission band of the hybrid, there existed four main excitation bands centered at 245 nm, 278 nm, 295 nm and 337 nm, respectively. The latter two bands can be considered as coming from ZnS_2L. The band centered at 278 nm was very close to that of bare ZnS particles, which revealed that there existed ZnS component in the hybrid. The band at 245 nm can be considered as a newly formed fragment from ZnS particles and ZnS_2L at the interface.

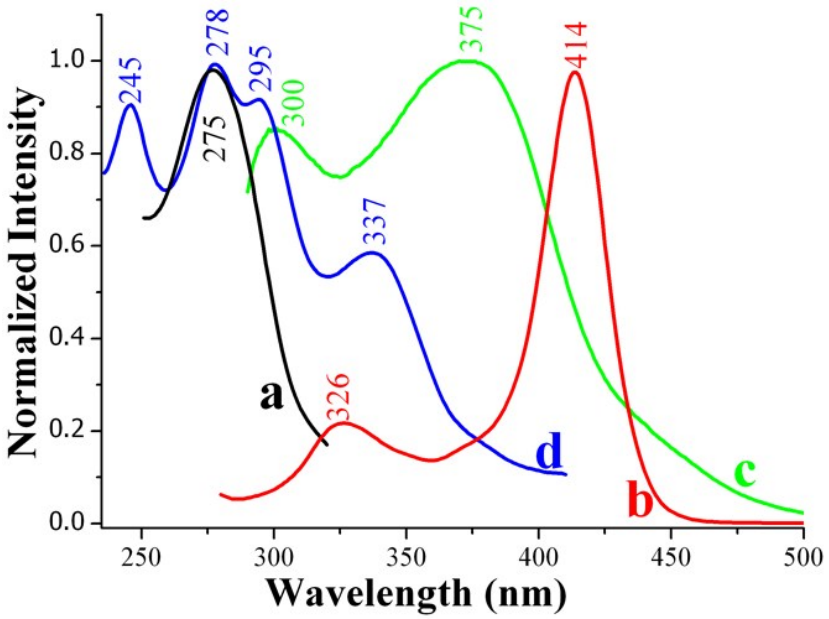

Figure S11 PLE spectra for (a) bare ZnS at 375 nm emission, (b) ZnS_2L at 528 nm emission, (c) the hybrid at 522 nm emission and (d) the hybrid at 416 nm emission. The samples were dispersed in EtOH-H_2O mixed solution with water fraction *f*w = 90%.

To make sure the interfacial interactions between ZnS_2L and ZnS components, ZnS_2L-EtOH solution was added into Zn^{2+}-water solution with the nZn^{2+}:$nZnS_2L$ molar ratio being 2.0 (EtOH-H_2O mixed solvent with the water fraction being 90%), the ratio was captured from UV-vis titration data Fig. S10. The samples were stayed undisturbed overnight before the examination. The PL spectra, PL excitation spectra, and PL decay traces were then studied.

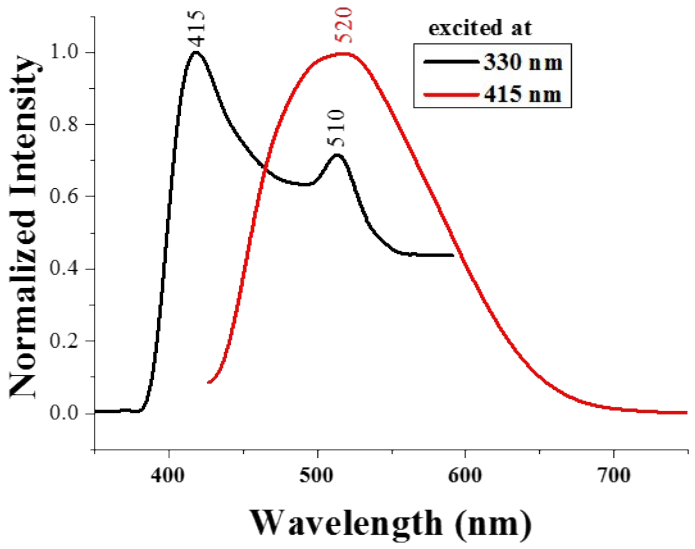

Figure S12 SPEF spectra of ZnS_2L in Zn^{2+} solution under 330 nm and 415 nm excitation, the sample was dispersed in EtOH-H_2O mixed solution with *f*w = 90%. The molar ratio of ZnS_2L to Zn^{2+} was 1:2.

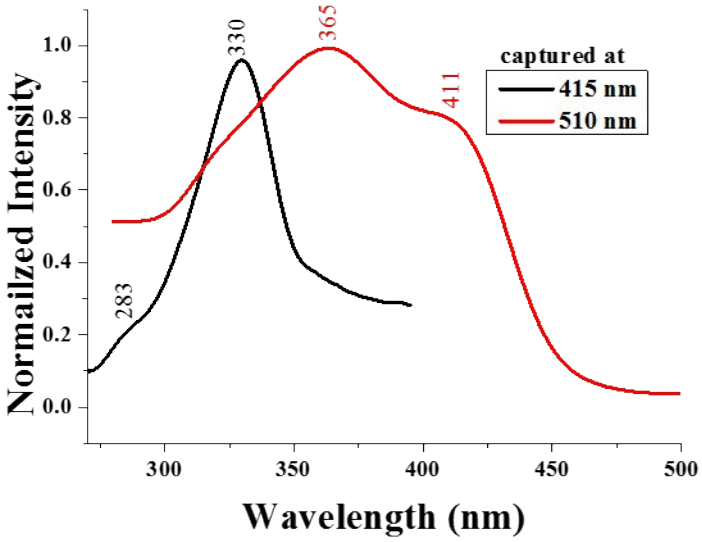

Figure S13 PLE spectra for ZnS_2L in Zn^{2+} solution captured at 510 nm and 415 nm emission, the sample was dispersed in EtOH-H_2O mixed solution with *f*w = 90%. The molar ratio of ZnS_2L to Zn^{2+} was 1:2.

When the mixed solution was excited at 330 nm, there appeared two main emission bands centered at 415 nm and 510 nm, respectively. For 510 nm emission band, the corresponding excitation bands centered at 365 nm and 411 nm. The data was similar with that of free ZnS_2L, which meant that 510 nm emission band came from the ZnS_2L component in the mixture. For 415 nm emission band, the related excitation bands

located at 330 nm with a shoulder band at 283 nm. The 330 nm excitation band was similar to that of the ZnS-ZnS_2L hybrid particles (337 nm) as shown in Figure S11d, which meant that the 415 nm emission band of the hybrid as well as the Zn^{2+}-ZnS_2L mixture may come from the newly formed species at the interface and/or in the mixture. The result also meant that the interactions between ZnS nanoparticles and ZnS_2L complex in the hybrid was between Zn^{2+} ions and ZnS_2L molecules at the interface. The newly formed emission band of the hybrid centered at 416 nm was come from the new species of the interfacial Zn^{2+}-ZnS_2L. That is to say, the coordination effect between Zn^{2+} ions and ZnS_2L molecules at the interface of the hybrid gives rise to the tunable single photon optical properties.

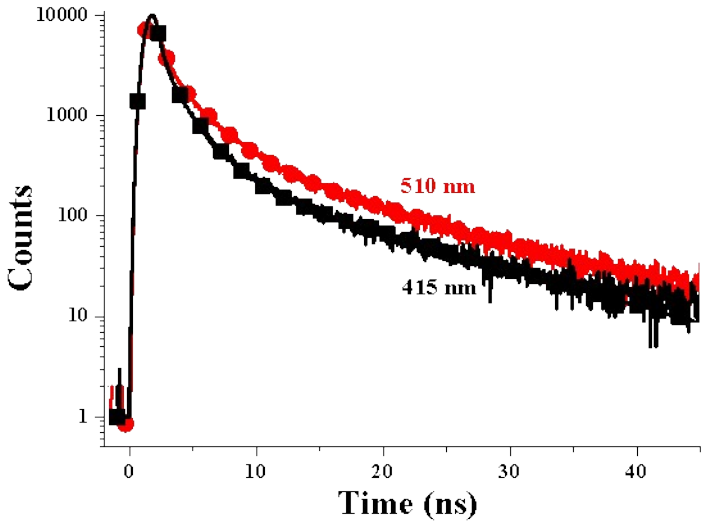

Figure S14 Time-domain fluorescence intensity decay (Ex: 370 nm) of ZnS_2L in Zn^{2+} solution monitored at 510 nm, and 415 nm. The molar ratio of ZnS_2L to Zn^{2+} was 1:2. The samples were dispersed in EtOH-H_2O mixed solution with *f*w = 90%.

Table S1 Fluorescence decay lifetime (τ) and amplitude (A) of ZnS_2L and the hybrid

	λ (nm)	τ1(ns)	A1(%)	τ2(ns)	A2(%)	τ3(ns)	A3(%)	$\bar{\tau}$	χ2	K_f 10^8s^{-1}	K_i 10^8s^{-1}
ZnS_2L	528	1.69	78	2.68	22	-	-	1.89	1.38	1.746	3.545
the	416	0.67	78	2.86	16	17.45	6	2.00	1.09	1.0	4. 0
hybrid	522	2.41	24	6.30	2	0.33	74	0.97	1.52	2.062	8.247
ZnS_2L	415	0.34	86	1.97	13	11.54	1	0.66	1.38	-	-
$+Zn^{2+}$	510	2.49	15	0.42	83	12.06	2	0.94	1.40	-	-

Fluorescence decay profile measurements were carried out to study the difference of the spectral features between ZnS_2L and the hybrid. The experimental results were shown in Fig. 3 (h)-(k). The fluorescence decay lifetimes and amplitude were summarized in Table S1. The samples were monitored at proper emission wavelength. The average FL lifetime of the hybrid at the emission wavelength being 522 nm was 0.97 ns, which was shorter than that of free ZnS_2L (1.89 ns) at similar emission wavelength (528 nm). Combined with fluorescence quenching at 522 nm of the hybrid, the decrease in $\overline{\tau}$ suggested that the interactions between ZnS_2L and ZnS components in the hybrid increased the radiative rate, which resulted in faster decay and a shorter average fluorescence decay lifetime.

Moreover, the fluorescence of free ZnS_2L was found to decay with two components at the excited state, a short component had a decay lifetime of 1.68 ns (the corresponding amplitude is 78%), and the following component had 2.68 ns (A = 22%). However, the emission band of ZnS_2L showed only one peak, maybe the intensity of the other band overlapped the existing band or it appeared as a shoulder band.[S9-S10] While for ZnS_2L component in the excited state of the hybrid, there existed three components, the fluorescence decay lifetime and the corresponding amplitude of the short component were 2.41 ns and 24%, respectively. The decay lifetime of the following component was 6.30 ns with amplitude being 2%. It was worth noting that a short lifetime of 0.33 ns appeared for the excited state of the hybrid. The amplitude of this short component was about 74%. The results revealed the existence of the newly formed fluorescent fragment in the hybrid as discussed above. The third lifetime component with much shorter lifetime revealed the presence of an additional fast nonradiative decay channel. The interactions between ZnS_2L and ZnS components at the interface may be responsible for the phenomenon.

Fluorescence decay profile measurements were also carried out. The experimental results were shown in Fig. S14. The fluorescence decay lifetimes and amplitude were summarized in Table S1. The average FL lifetime of the Zn^{2+}-ZnS_2L mixture at the

emission wavelength being 510 nm was 0.94 ns, which was composed of three components in the excited state. The shortest component had a decay lifetime of 0.42 ns (the corresponding amplitude is 83%), the following component had 2.49 ns (A = 15%) and the third component had 12.06 ns with A = 2%. The appearance of the newly 0.42 ns component was agreed well with that of the ZnS_2L component in the hybrid (Fig. 3i). Combined with the above discussions of PL spectra and PLE spectra, it can be concluded that the existence of the newly formed fluorescent fragment in the hybrid was come from the interfacial Zn^{2+}-ZnS_2L interactions.

S6. Aggregation caused quenching (ACQ) effect of ZnS_2L

Compound ZnS_2L showed traditional ACQ effect in N,N-dimethylformamide (DMF)-water mixed solution with the concentration being kept at 1.0×10^{-5} mol·L^{-1}. ZnS_2L emitted strongly in pure DMF solution. The fluorescence intensity of ZnS_2L in the aggregate state was apparently weaker than that of the pure DMF solution. As seen in Fig. S13b, with an increasing content of water from 0 to 99 vol%, ZnS_2L showed a dramatic change of fluorescence intensity from the strongly isolated single molecule in DMF to the weak fluorescent nanoparticles suspension in DMF-water, which could be related to the aggregate formation. In the case of 50% volume fractions (*f*w) of water addition, the fluorescence intensity decreased drastically and reached the minmum value, with the intensity decreasement for about 98.6%. Further, the fluorescence intensity remained still until *f*w = 99%. The aggregate formation can also be observed from the UV-vis absorption spectra (Fig. S11a). The short- and long-wavelength bands in the UV-vis absorption spectra of ZnS_2L in DMF-water mixture were supposed to be due to the absorption from the carbazole species and from species of the whole molecule regions, respectively. With an increasing content of water from 0 to 99 vol%, the absorption band of carbazole unit remained at the same position of 292 nm, in general. However, with up to 40% volume fractions of water addition, the maximum absorption band of the whole molecule showed an obvious red-shift and reducement compared to that of dilute solution, due to the extension of the effective conjugation

lengths caused by the planarization of a molecule in the aggregated state. The long-wavelength absorption peak of ZnS_2L red shifted for about 31 nm from 373 nm to 404 nm when the *f*w increased from 0% to 90%, indicating a better conjugation degree in the water-induced aggregation. The formation of aggregates can also be concluded from the lifted level-off tail in the absorption spectra when the water volume fraction was 50% to 99%, which were attributed to Mie scattering caused by nanosized particles.

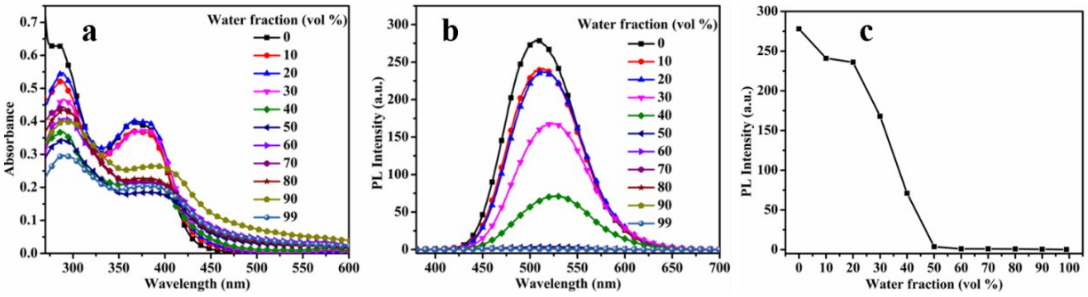

Figure S15 (a) UV-vis absorption and (b) PL emission spectra changes of ZnS_2L (1.0×10^{-5}mol·L^{-1}) in DMF-water mixtures with different water volume fractions; (c) the effect of water volume fraction (*f*w) on the maximum emission intensity of ZnS_2L in DMF-water with the concentration being 1.0×10^{-5} mol·L^{-1}.

S7. Two-photon excited fluorescence of ZnS_2L and the hybrid

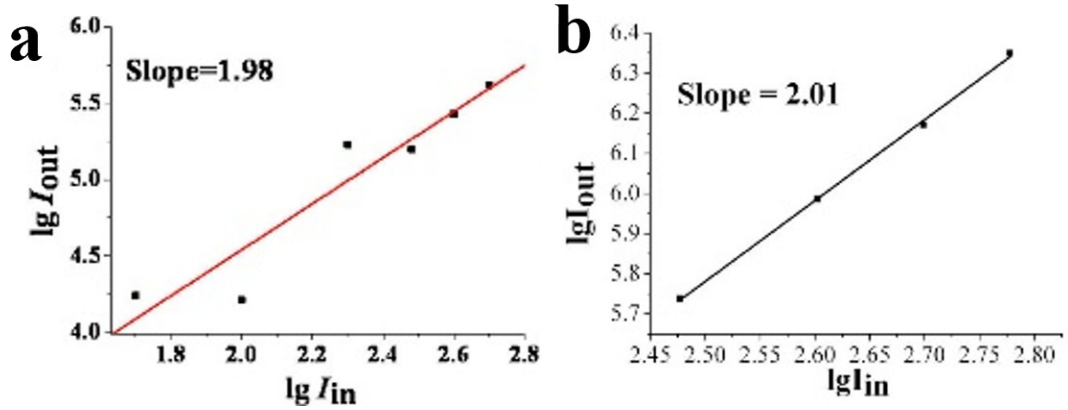

Figure S16 The logarithmic plots of the output fluorescence (I_{out}) *vs*. the square of input laser power (I_{in}) of (a) ZnS_2L and (b) the hybrid. The samples were dispersed in EtOH-H_2O mixed solution.

S8. Optical properties of $ZnS_2L@SiO_2$ nanohybrid

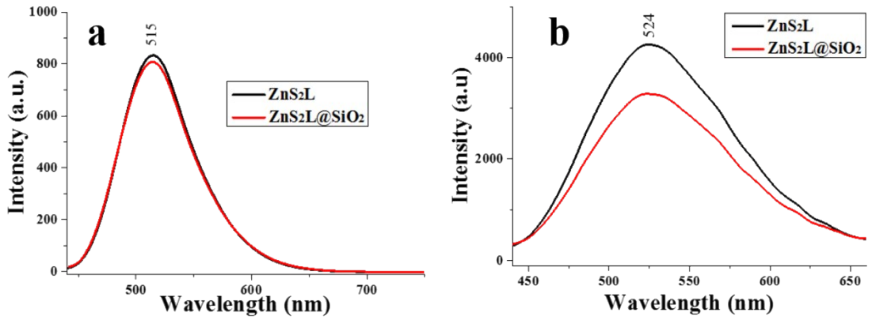

Figure S17 (a) Single-photon excited fluorescence and (b) two-photon excited fluorescence of ZnS_2L and the $ZnS_2L@SiO_2$ hybrid.

S9. Computational studies

To better understand the electronic structure and linear optical properties of ZnS_2L, molecular orbital calculations of TD-DFT at the B3LYP/6-31G(d,p) level basis set [S11] were performed. The molecular geometry used for the calculation was obtained from X-ray diffraction crystallographic data. The theoretical spectral characteristics, detailed information of ZnS_2L, shown in Table S2, showed one main transition (λ_{abs} = 412 nm), which was from the HOMO-6 orbit to the LUMO+1 (oscillator strength $f_{(HOMO-6)-(LUMO+1)}$ being 0.58407). There existed a main fluorescence band for ZnS_2L (λ_{FL} = 525 nm), which resulted from two transitions. One was from the LUMO orbit to the HOMO-5 (oscillator strength $f_{(LUMO)-(HOMO-5)}$ being 0.31504). The other was from LUMO+2 orbit to the HOMO-3 (oscillator strength $f_{(LUMO+2)-(HOMO-3)}$ being 0.44699). The calculated results fit with the experimental data. Meanwhile, the calculated results did not show any absorption at 352 nm, nor any fluorescence band at 416 nm.

Considering the description of the preceding analysis, it can be concluded that the newly formed absorption band and fluorescence band of the hybrid were the inherent characteristic of the newly formed flueroscent fragment between ZnS_2L and ZnS components in the hybrid, which was comfirmed from the UV-vis titration experiment.

Table S2 Some of calculated excitation energies (E), oscillator strengths (f), corresponding wavelengths (λ_{abs}) and major contributors for ZnS_2L

	E (eV)	λ (nm)	f	composition (C)
absorbance	2.8856	429.67	0.0005	175(H-2) →181(L+3) (0.65493)
	2.9501	420.28	0.0094	176(H-1) →182(L+4) (0.60385)
	3.0045*	412.66	0.0261	171(H-6) →179(L+1) (0.58407)
	3.0301	409.17	0.0009	175(H-2)→182(L+4) (0.63133)
fluorescence	2.3594*	525.48	0.0803	178(L) →172(H-5) (0.31504)
				180(L+2) →174(H-3) (0.44699)

* main transition

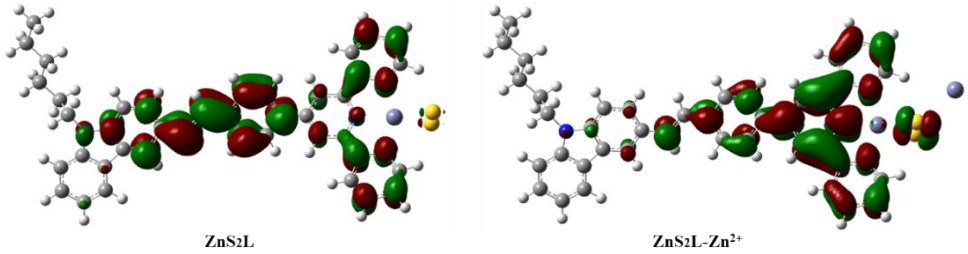

Figure S18 Molecular orbital diagrams of LUMO of optimized ZnS_2L molecule and Zn^{2+} coordinated ZnS_2L (the geometry was optimized using the B3LYP functional and the 6-31G* basis set) according to TD-DFT calculation.

Reference

[S1] a) C. Xu, W. W. Webb, *J. Opt. Soc. Am. B,* **1996**, *13*, 481; b) A. Ajami, W. Husinsky, R. Liska, N. Pucher, *J. Opt. Soc. Am. B,* **2010**, *27*, 2290;

[S2] D. M. Li, Q. Zhang, A. M. S. Hossain, M. Sun, J. Y. Wu, J. X. Yang, H. P. Zhou, L. M. Tao, C. K. Wang, Y. P. Tian, *Sci. Chin. Chem.,* **2010**, *54*, 730;

[S3] O. Varnavski, T. Goodson, L. Sukhomlinova, R. Twieg, *J. Phys. Chem. B,* **2004**, *108*, 10484;

[S4] X. C. Wang, X, H. Tian, Q. Zhang, P. P. Sun, J. Y. Wu, H. P. Zhou, B. K. Jin, J. X. Yang, S. Y. Zhang, C. K. Wang, X. T. Tao, M. H. Jiang, Y. P. Tian, *Chem. Mater.*, **2012**, *24*, 954;

[S5] Q. F. Zhang, J. H. Ding, Z. Yu, Y. L. Song, A. Rothenberger, D. Fenske, W. H. Leung, *Inorg. Chem.,* **2006**, *45*, 8638;

[S6] D. S. Correa, L. De Boni, L. Misoguti, I. Cohanoschi, F. E. Hernandez, C. R. Mendonca, *Opt. Commun.,* **2007**, *277*, 440;

[S7] D. M. Li, Q. Zhang, A. M. S. Hossain, M. Sun, J. Y. Wu, J. X. Yang, H. P. Zhou, L. M. Tao, C. K. Wang, Y. P. Tian, *Sci. Chin. Chem.,* **2010**, *54*, 730;

[S7] W. B. Wu, Z. Xu, Y. Xiong, S. H. Xin, H. D. Tang, C. Ye, G. F. Qiu, J. G. Qin and Z. Li, *New J. Chem.***, 2013**, *37*, 1789;

[S8] S. Goswami, S. Das, K. Aich, Tetrahedron Letters *2013*, **54**, 4620;

[S9] a) W. B. Wu, Z. Xu, Y. Xiong, S. H. Xin, H. D. Tang, C. Ye, G. F. Qiu, J. G. Qin and Z. Li, *New J. Chem.*, **2013**, *37*, 1789;

[S10] F. Stellacci, C. A. Bauer, T. Meyer-Friedrichsen, W. Wenseleers, S. R. Marder, J. W. Perry, *J. Am. Chem. Soc.,* **2003**, *125*, 328;

[S11] M. J. G. W. T. Frisch, H. B. Schlegel, G. E. Scuseria, M. A. Robb, J. R. Cheeseman, G. Scalmani, V. Barone, B. Mennucci, G. A. Petersson, H. Nakatsuji, M. Caricato, X. Li, H. P. Hratchian, A. F. Izmaylov, J. Bloino, G. Zheng, J. L. Sonnenberg, M. Hada, M. Ehara, K. Toyota, R. Fukuda, J. Hasegawa, M. Ishida, T. Nakajima, Y. Honda, O. Kitao, H. Nakai, T. Vreven, J. A. Montgomery, Jr., J. E. Peralta, F. Ogliaro, M. Bearpark, J. J. Heyd, E. Brothers, K. N. Kudin, V. N. Staroverov, R. Kobayashi, J. Normand, K. Raghavachari, A. Rendell, J. C. Burant, S. S. Iyengar, J. Tomasi, M. Cossi, N. Rega, J. M. Millam, M. Klene, J. E. Knox, J. B. Cross, V. Bakken, C. Adamo, J. Jaramillo, R. Gomperts, R. E. Stratmann, O. Yazyev, A. J. Austin, R. Cammi, C. Pomelli, J. W. Ochterski, R. L. Martin, K. Morokuma, V. G. Zakrzewski, G. A. Voth, P. Salvador, J. J. Dannenberg, S. Dapprich, A. D. Daniels, O. Farkas, J. B. Foresman, J. V. Ortiz, J. Cioslowski and D. J. Fox, *Gaussian 09, Revision B. 01***.** Gaussian, Inc., Wallingford CT. **2009**.